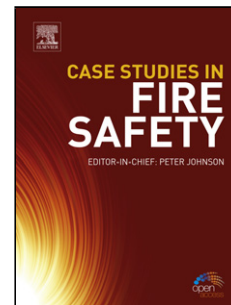# Accepted Manuscript

Title: Active corrosion protection by a smart coating based on a MgAl-layered double hydroxide on a cerium-modified plasma electrolytic oxidation coating on Mg alloy AZ31

Authors: Gen Zhang, Liang Wu, Aitao Tang, Yanlong Ma, Guang-Ling Song, Dajiang Zheng, Bin Jiang, Andrej Atrens, Fusheng Pan

Please cite this article as: Zhang G, Wu L, Tang A, Ma Y, Song G-Ling, Zheng D, Jiang B, Atrens A, Pan F, Active corrosion protection by a smart coating based on a MgAl-layered double hydroxide on a cerium-modified plasma electrolytic oxidation coating on Mg alloy AZ31, *Corrosion Science* (2010), https://doi.org/10.1016/j.corsci.2018.05.010

This is a PDF file of an unedited manuscript that has been accepted for publication. As a service to our customers we are providing this early version of the manuscript. The manuscript will undergo copyediting, typesetting, and review of the resulting proof before it is published in its final form. Please note that during the production process errors may be discovered which could affect the content, and all legal disclaimers that apply to the journal pertain.

Active corrosion protection by a smart coating based on a MgAl-layered double hydroxide on a cerium-modified plasma electrolytic oxidation coating on Mg alloy AZ31

Gen Zhang [a], Liang Wu [a,b]*, Aitao Tang [a,b]**, Yanlong Ma [c], Guang-Ling Song [d], Dajiang Zheng [d], Bin Jiang [a,b], Andrej Atrens [e], Fusheng Pan [a,b]

[a] College of Materials Science and Engineering, Chongqing University, Chongqing 400044, China.

[b] National Engineering Research Center for Magnesium Alloys, Chongqing University, Chongqing 400044, China.

[c] College of Materials Science and Engineering, Chongqing University of Technology, Chongqing 400054, China.

[d] Center for Marine Materials Corrosion and Protection, State Key Laboratory of Physical Chemistry of Solid Surface, College of Materials, Xiamen University, Xiamen 361005, China.

[e] School of Mechanical and Mining Engineering, The University of Queensland, Brisbane Qld 4072, Australia.

* Dr. Liang Wu E-mail address: wuliang@cqu.edu.cn.

** Prof. Aitao Tang E-mail address: tat@cqu.edu.cn.

Highlights

- PEO with Ce salt sealing and LDHs composite film was produced via hydrothermal treatment and was then modified by phytic acid.

- *PEO-Ce-LDH* showed two different surface morphologies.

- Due to the compact insoluble precipitate covered the entire defect, *PEO-Ce-LDH-P* had the best self-healing ability.

ABSTRACT:

A composite coating was produced via (i) plasma electrolytic oxidation (PEO) with Ce salt sealing, on which layered double hydroxides (LDHs) were deposited via a hydrothermal treatment, and (ii) then modified by phytic acid (PA) *via* an ion-exchange reaction. The final coating (characterized using XRD, XPS, FT-IR, SEM, EDS and GDOES) consisted of $LDHs/Mg(OH)_2/CeO_2/Ce(OH)_3$ with a non-uniform Ce distribution. The corrosion protection and self-healing ability were investigated using polarization curves, EIS, immersion tests and SVET. The composite coating modified with PA showed the most superior corrosion protection and self-healing ability, attributed to the synergistic effect between Ce species and phosphate.

1. Introduction

Nowadays, application of protective coating is a widespread and cost-effective approach to corrosion protection for metallic substrates. The main role of the protective coating in corrosion protection is to provide a physical barrier for avoiding contact with the corrosive medium [1,2]. However, in the case of a defect, these coatings can often cause severe localized corrosion. Therefore, the concept of a smart coating has been proposed that has some functionality in addition to being a conventional barrier coating. Such a smart coating has an imbedded system that is capable of a response when the coating is subjected to stimuli from the environment, such as pH, aggressive species, breakdown by mechanical damage, dissolution, humidity or moisture [3].

Self-healing coatings are a recently developed class of smart coatings, in which minor damage or defects are actively repaired by the coating without the need for any external intervention [4]. Usually, the self-healing ability is achieved by introducing corrosion inhibitors into the coating. Corrosion inhibitors can diffuse to the exposed metallic surface around the defect, and interact with the metallic substrate to form stable precipitates on the defect. As a result, the defect can be healed in such a way. The traditional manner of using corrosion inhibitors is to directly mix the corrosion inhibitor with the binder, which makes up the coating. However, the following problems are likely: (i) poor dispersion of the corrosion inhibitor throughout the coating, and (ii) the interaction between the corrosion inhibitor and the polymer substrate. Both these problems influence the release kinetics of the corrosion inhibitor,

and likely lead to poor inhibition, or even lack of functionality.

Encapsulation strategies have been widely proposed in order to avoid such problems, e.g. by White *et al.* [5]. In their study, the microcapsules included a healing agent (dicyclopentadiene, DCPD) and Grubbs' catalyst particles, and were embedded into a structural polymeric material, to achieve a superior self-healing effect. Subsequently, there has been significant development of the encapsulating technology for corrosion inhibitors. Encapsulation has the following advantages over the traditional approach: (i) the corrosion inhibitor may be easily leached from the coating, (ii) the encapsulation can be designed so that the corrosion inhibitor is released by some trigger and (iii) encapsulation may provide a long-term healing effect of induced defects and consequently may provide long-term protection of the metallic substrate [3]. Examples of encapsulating containers are: (i) inert capsules which play no role other than to isolate the corrosion inhibitor from the polymeric material, and (ii) ion exchange materials which release the corrosion inhibitors in exchange for aggressive ions (e.g. chloride ions). Zhang *et al.* [6] developed a copper (II) 8-hydroxyquinolinate ($Cu(8HQ)_2$) 3D network container, which they loaded with benzotriazole (BTA). They showed that the BTA embedded in the 3D network structure was rapidly released from the composite coating to inhibit corrosion when the coating was scratched. To increase the amount of corrosion inhibitor released, inorganic nanocarriers SiO_2 were coated with polyelectrolyte shells assembled by the Layer-by-Layer (LbL) technique, and BTA was then incorporated between oppositely charged polyelectrolyte layers. When corrosion was about to start or had already

started, the triggered release of the BTA was achieved using the permeability

dependence of the polyelectrolyte shell on pH to provide release of the corrosion

inhibitors [7,8].

Furthermore, layered double hydroxides (LDHs) have been widely investigated as

nanocarriers because of their excellent ion-exchange capability [9-13]. Tedim *et al.*

[14] found that LDHs nitrate produced effective chloride nanotraps, and were

sensitive to the chloride concentration in the bulk solution. Moreover, LDH

nanocarriers loaded with corrosion inhibitor can play a double role: (i) entrapment of

aggressive anionic species such as Cl^- and (ii) a triggered release of anionic corrosion

inhibitors [15]. The schematic representation of an ion-exchange reaction is shown as

Fig. 1.

Recently, attempts to combine a LDH coating with a plasma electrolytic oxidation

(PEO) coating on aluminium (Al) have become a rapidly growing research area. The

production of the LDHs on the PEO coating can seal the pores of the PEO coating,

which improves the corrosion protection provided by the PEO coating for the

substrate. In addition, the LDHs can store and release inhibitors, and thus provide the

function of a self-healing, protective, corrosion retarding coating. Dou *et al.* [16]

reported that the LDH growth occurs preferentially (i) on the bumpy areas of the PEO

coating with high specific surface area, (ii) on areas of complicated composition, and

(iii) on γ-Al_2O_3 rather than on α-Al_2O_3. Moreover, Serdechnova and Mohedano [17]

grew ZnAl-LDH nanocontainers *in-situ* on the surface and in the pores of the PEO

layer, vanadate ions were then intercalated into them. The results showed that such a

sealing improved the corrosion resistance and vanadate-containing LDHs can effectively heal the defects, suppressing corrosion. They further investigated the effect of the voltage used to produce the PEO on the growth of LDHs, and found that coatings produced at higher voltages had a decreased number of LDH flakes on the surface of the PEO layers [18].

However, the above publications were based on Al alloys, and the study of PEO coatings on magnesium (Mg) alloys modified with LDHs is still limited. Our previous works proposed an easy approach to growing MgAl-LDHs on the anodized Mg alloy AZ31 [19,20]. The obtained results showed that MgAl-LDHs fabricated on the anodic layer provided good protection of the Mg substrate against corrosion. With this method, MgAl-LDHs were produced on the surface of the PEO treated Mg alloys in the present work. Furthermore, there is a growing demand for corrosion inhibitors that are less toxic or not toxic and are more biodegradable [21]. Usually, cerium (Ce) was selected to seal the porous PEO layer, providing a higher corrosion resistance [22,23]. Moreover, Ce as a rare earth (RE) inhibitor has been proven [24]. Therefore, Ce was selected herein to pre-treat the porous PEO layer on the Mg alloy in order to obtain a strongly self-healing and corrosion protective composite coating. Moreover, Chen *et al.* [10] reported modification of LDHs using environment-friendly corrosion inhibitor phytic acid (PA) solution. Hence, in this work phosphate from the PA solution was intercalated into the LDH galleries *via* an ion-exchange reaction after the deposition of the LDHs on the PEO layer modified with a cerium conversion coating (CCC). The resulting coatings were investigated using XRD, XPS, SEM, EDS, FT-IR and

GDOES. The corrosion performance was evaluated using Tafel extrapolation of

polarization curves, EIS, immersion tests, and the localized electrochemical

technique, scanning vibrating electrode technique (SVET).

2. Experimental Methods

2.1 Materials

The Mg alloy AZ31 had the nominal composition of Al 2.5-3.5%, Zn 0.6-1.3%,

Mn 0.2-1%, Ca 0.04%, Si 0.1%, Cu 0.05% (all in wt.%), and balance Mg. Deionized

water was used as the solvent.

2.2 Specimens preparation

The specimens with size of 20 mm × 20 mm × 5 mm were ground to 2000 grit

using SiC papers on all surfaces, ultrasonically cleaned in ethyl alcohol, and then

dried in warm air. The PEO coating was produced for 600s using a pulsed AC power

supply with a square electrical signal (100 Hz, + 250 V/ - 50 V, 26%). The frequency

and duty ratio were 100 Hz and 26%, respectively. The electrolyte, containing 7.14

g/L NaOH and 4 g/L $NaAlO_2$, was continuously stirred and the temperature of

electrolyte was maintained at 25 ± 5 °C by a self-made water cooling system. The

obtained PEO treated specimens were designated as *PEO*. Subsequently, the as-

prepared *PEO* specimens were cerium conversion coated by immersion in the

aqueous solution containing 5 g/L $Ce(NO_3)_3$ and 0.5 g/L H_2O_2 at 50 °C for 2 h in a

water bath, and these specimens were designated as *PEO-Ce*.

The MgAl-LDH coating on the *PEO-Ce* specimens were produced by treatment

of the specimens hydrothermally in 0.1 M $NaNO_3$ solution in a Teflon-lined stainless

steel autoclave at 398 K for 12 h. These specimens were designated as *PEO-Ce-LDH*.

Phosphate anion loading was performed by immersion of the *PEO-Ce-LDH*

specimens into the 40 mL/L PA aqueous solution of pH 11 at 80 °C for 1 h. The pH of

the PA aqueous solution was adjusted using 2 M NaOH. These specimens were

designated as *PEO-Ce-LDH-P*.

2.3 Characterization

   The crystallographic structure was studied using X-ray diffraction (XRD; Rigaku

D/Max 2500X, Japan) using a Cu target (40 kV, 150 mA) at a glancing angle of 1.5°,

within the range of $2\theta = 5 - 80°$ and at a scanning rate of $4°$ min^{-1}. Fourier transform

infrared spectra (FT-IR; Thermo Scientific Nicolet IS5, US) were obtained in the

range of 4000-400 cm^{-1}. Surface and cross-sectional morphologies of the specimens

were investigated using field emission scanning electron microscopy (FE-SEM; JEOL

JSM-7800F, Japan). For cross-sectional examination, sections of the specimens were

generated by ultramicrotomy (UC; Leica EM UC7, Germany) using a diamond knife.

The chemical composition of the LDH coatings was evaluated using energy

dispersive spectroscopy (EDS; Oxford INCA Energy 350, UK) and X-ray

photoelectron spectroscopy (XPS; Thermo Scientific ESCALAB 250Xi, US) with Al

K_α radiation (1486.6 eV). Glow discharge optical emission spectroscopy (GDOES;

Horiba Scientific GD Profile 2, French) depth profile analysis was carried out at a

pressure of 700 Pa and at a power of 40 W.

   Polarization curves and electrochemical impedance spectra (EIS) were measured

using a three-electrode cell with a saturated calomel reference electrode, a platinum

8

counter electrode and the coated Mg substrate as the working electrode.

Electrochemical measurements were performed using a CIMPS-2 Zahner system. The

polarization curves were recorded from -2.0 V_{SCE} to 0.5 V_{SCE} at a sweep rate of 1 mV

s^{-1}. The impedance measurements used a sine signal with an amplitude of 10 mV. The

range of measured frequencies extended from 0.01 Hz to 100 kHz, with a logarithmic

sweep of 7 points per decade. All the spectra were recorded at the open circuit

potential. The experimental impedance plots were fitted to equivalent circuits using

the Zview software. The scanning vibrating electrode technique (SVET)

measurements were performed using Bio-Logic Uniscan M470. The vibrating

microelectrode vibrated at 80 Hz with an amplitude of 30 μm at an average distance

of 200 μm from the surface of the specimens. Each scan consisted of 100×100 points

and took about 20 minutes. Artificial defects, whose length was approximately 10

mm, were introduced into the coated specimens by a sharp knife.

3. Results and Discussion

3.1 Structure, composition and morphology

XRD patterns of *PEO*, *PEO-Ce*, *PEO-Ce-LDH* and *PEO-Ce-LDH* specimens are

presented in Fig. 2. The *PEO* coating was composed of MgO and Al_2O_3. Treatment in

the Ce containing solution produced the diffraction peaks corresponding to CeO_2.

Valdez *et al.* [21] and Scholes *et al.* [25] also detected cerium in the 3-valence state

($Ce(OH)_3$) after treatment in a Ce containing solution. No obvious diffraction peaks

corresponding to $Ce(OH)_3$ herein may be attributed to the fact that the Ce(III)

hydroxide was present in an amorphous form. Production of the LDHs on the *PEO-Ce*

produced the diffraction peaks characteristic of LDHs, corresponding to the 003 and 006 planes [26]. The intensity of the (00l) reflection family (l = 3 and 6) had contributions by diffraction from both the LDH host layers containing Mg or Al cations coordinated octahedrally by hydroxyl groups and the interlayer anions [27]. Wang *et al.* [28] and Zhang *et al.* [29] had also reported the presence of the MgAlCe-LDHs and the ZnAlCe-LDHs in their studies, respectively. Wang *et al.* [28] suggested that the intercalation of Ce into the LDH layers can result in a large distortions of the LDH layers and a decrease in the crystallinity because of the large ionic radius of Ce. Fig. 2 shows a weaker crystalline structure for LDHs in *PEO-Ce-LDH*, which may indicate the presence of some MgAlCe-LDHs in *PEO-Ce-LDH*. Moreover, the original sharp peak of CeO_2 at about 28° changed to a hump peak. Usually, a hump peak is related to an amorphous phase [30]. Therefore, this result implies that the crystallinity of the CeO_2 decreased after the growth of the LDHs. Moreover, the peaks of $Mg(OH)_2$ were also visible. After the ion-exchange process in the PA solution, characteristic reflections 003 and 006 shifted toward lower angles, indicating phosphates were intercalated into LDH the interlayer successfully.

In order to further understand the change processes of cerium and the interlayer anions before and after treatment, sensitive XPS were measured for *PEO-Ce*, *PEO-Ce-LDH* and *PEO-Ce-LDH*. High resolution XPS spectra for the different specimens for (a) Ce 3d; (b) O1s; (c) N 1s and (d) P 2p are presented in Fig. 3. For the Ce^{4+}, the split $3d_{5/2}$ and $3d_{3/2}$ core holes were usually consisted of two multiplets, namely *v, v″, v‴* and *u, u″, u‴*, which have already been reported [31-33]. The peaks *v u* and *v″ u″*

10

were the results of Ce $3d^94f^2$ O $2p^4$ and Ce $3d^94f^1$ O $2p^5$ states respectively. The peaks

v''' and u''' were attributed to a Ce $3d^94f^0$ O $2p^6$ state. For Ce^{3+}, the Ce $3d_{3/2}$ and $3d_{5/2}$

spectra were also usually composed of two multiplets, namely v^0, v' and u^0, u'. The

peaks v^0 and u^0 are attributed to a Ce $3d^94f^2$ O$2p^5$ final state. The peaks v' and u' are

attributed to a Ce $3d^94f^1$ O$2p^6$ final state [34]. Because of the lack of the Ce $4f^0$

configuration for Ce^{3+}, the satellite peak u''' corresponding to Ce $3d_{3/2}$ is characteristic

of the presence of Ce^{4+} in Ce compounds [35]. This clearly shows that the presence of

two valence states for cerium in Ce 3d core level (Fig. 3a): Ce (III) and Ce (IV),

which was consistent with the literature [36]. The binding energy (B. E.) of the peaks

are listed in Table 1.

Moreover, the amounts of Ce (IV) and Ce (III) can be calculated from the Ce 3d

core level using the following equations [37]:
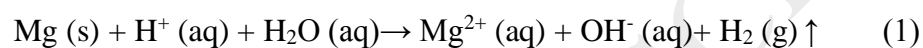
Ce (IV) $= v + u + v'' + u'' + v''' + u'''$

Ce (III) $= v^0 + u^0 + v' + u'$

Ce (IV) $= \frac{Ce(IV)}{Ce(IV)+Ce(III)} \times 100\%$

Ce (III) $= \frac{Ce(III)}{Ce(IV)+Ce(III)} \times 100\%$

The respective peak area ratio and the calculated amounts of Ce(IV) and Ce(III) are

listed in Table 1. These results show that *PEO-Ce* contained cerium mainly in the 4-

valence state (CeO_2, 79%), while the content of CeO_2 decreased to 59% in *PEO-Ce-*

LDH and 61% in *PEO-Ce-LDH-P*. This decrease can be attributed to the

decomposition of CeO_2, which is in agreement with the XRD results (Fig. 2). In our

previous unpublished study, we found that the LDH coating simultaneously grew in

opposite directions, i.e., outwards growth to the coating/solution interface and inwards

growth to the Mg substrate. The dissolution of the Mg substrate and interaction with

other reactants lead to such an inwards growth. As a result, some Mg loses electrons

and is oxidized to Mg^{2+}, some Ce^{4+} and H^+ receives electrons and is reduced to Ce^{3+}

and H_2 respectively, and because of the accumulation of OH^- ions, $Mg(OH)_2$ and

$Ce(OH)_3$ are formed. This result agrees with the XRD analyses. The chemical

reactions are described as follows [38,39]:

$$Mg\ (s) + H^+\ (aq) + H_2O\ (aq) \rightarrow Mg^{2+}\ (aq) + OH^-\ (aq) + H_2\ (g) \uparrow \qquad (1)$$

$$Ce^{4+}\ (aq) + e^- \rightarrow Ce^{3+}\ (aq) \qquad (2)$$

$$Mg^{2+}\ (aq) + 2OH^-\ (aq) \rightarrow Mg(OH)_2\ (s) \downarrow \qquad (3)$$

$$Ce^{3+}\ (aq) + 2OH^-\ (aq) \rightarrow Ce(OH)_3\ (s) \downarrow \qquad (4)$$

In addition, the Ce^{3+} could diffuse into the layers of the LDHs resulting in the

formation of a small amount of MgAlCe-LDHs, which is consistent with the above

XRD analysis and the following SEM result. Moreover, the Ce content (associated

with peak intensity) decreased after the ion-exchange reaction.

The spectrum of N 1s only displayed one peak at 400 eV, corresponding to NO_3^-.

After the ion-exchange reaction, the spectrum of P 2p exhibited a binding energy at

132.8 eV, indicating the presence of a phosphorus compound in the 5-valence

oxidation state and obviously as a P–O bonded species in LDH interlayer [40].

Fig. 4 presents the FT-IR spectra. The absorption bands at approximately 3693 and

3448 cm^{-1} are ascribed to the stretching vibration of H–O–H and the symmetric

contraction of O–H in the hydroxyls groups, respectively [10,41]. The absorption

band at 1640 cm^{-1} corresponds to the interlayer water molecules and the adsorbed water molecules on the surface [42]. In *PEO*, the band corresponding to CO_3^- can be attributed to the surface contamination. The bands in *PEO-Ce* and *PEO-Ce-LDH* corresponding to NO_3^- are the result of surface absorption of nitrate from the $Ce(NO)_3$ solution and the interlayer nitrate in the LDHs, respectively. After the ion-exchange reaction, there was a new band at 1058 cm^{-1} assigned to PO_4^{3-}, which indicated that the inhibitor PO_4^{3-} was intercalated into the LDH interlayer galleries successfully [10]. It is worth noting that NO_3^- was not fully displaced by PO_4^{3-}. Alibakhshi *et al.* [43] also had a similar finding in their study.

Fig. 5 shows the surface morphologies of the different specimens. Fig. 5a shows that the entire surface of *PEO* was smooth. Fig. 5b, at higher magnification, reveals a characteristic surface morphology of the PEO layer, composed by pores and micro-cracks [44]. The formation of such a typical morphology was caused by the gas evolution through the molten oxide during the PEO process and the thermal stresses at the sites of the discharge channels [45]. Fig. 5d shows a cracked dry mud-like structure, the initial pores have disappeared and the entire surface was covered with cerium-rich nodules, which was in agreement with Rivera' findings [33]. Valdez *et al.* [21] suggested that the initial formation of CCC was attributed to the deposition of small particles, occasionally cracked. With increasing reaction time, small particles grew and integrated to form larger particles. Therefore, there were different sized spherical particles (nodules). Hu *et al.* [46] reported that only a long treatment period in Ce-containing solution could result in the formation of cracks, and that the cracks

13

are the result of stress relief, which is due to the faster deposition rate of the CCC.

Moreover, the following CCC growth process has been proposed. Adding H_2O_2 can

result in the alkalization of Ce salt solution:

$$H_2O_2 \text{ (aq)} + 2e^- \rightarrow 2OH^- \text{ (aq)} \tag{5}$$
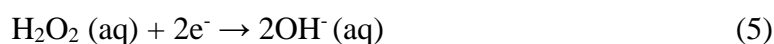
The accumulation of OH^- ions generated in reaction (5) results in an increase of pH.

As is well known, weak acidic, neutral, or alkaline baths are not suitable for Ce salts

because of their high hydrolysis tendency. For example, when $[Ce^{3+}]$ is 0.05 M, pH

must be lower than 3.6 [24]. Therefore, the increasing pH causes the precipitation of

Ce hydroxides on the surface of PEO layer:

$$Ce^{3+} \text{ (aq)} + 3OH^- \text{ (aq)} \rightarrow Ce(OH)_3 \text{ (s)} \downarrow \tag{6}$$

The H_2O_2 also plays an additional role as an oxidant, interacting with Ce^{3+} and

leading to Ce^{3+} being oxidized to Ce^{4+} in solution by the formation of a complex:

$$2Ce^{3+} \text{ (aq)} + H_2O_2 \text{ (aq)} + 2OH^- \text{ (aq)} \rightarrow 2Ce(OH)_2^{2+} \text{ (aq)} \tag{7}$$
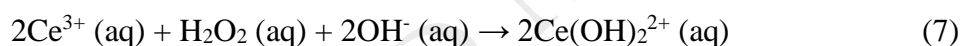
Further reaction leads to the formation of the CCC mainly composed by CeO_2, which

was consistent with XPS analyses, by following reactions:

$$2Ce(OH)_2^{2+} \text{ (aq)} + 2 OH^- \text{ (aq)} \rightarrow CeO_2 \cdot H_2O \text{ (s)} + H_2O \tag{8}$$

$$2Ce(OH)_2^{2+} \text{ (aq)} + 2 OH^- \text{ (aq)} \rightarrow CeO_2 \text{ (s)} + 2H_2O \tag{9}$$

Fig. 5e presents the SEM morphology of *PEO-Ce-LDH*. There were two different

surface morphologies in the *PEO-Ce-LDH*, which are marked as zone 1 and zone 2.

The higher resolution micrographs of zone 2 in Fig. 5g shows a typical flake-like

LDH structure. Fig. 5f shows that zone 1 contains circular or hexagonal flake-like

structures, which are similar to the typical structure of LDHs. Wang *et al.* [28]
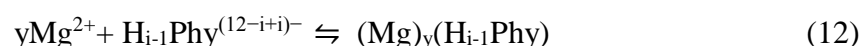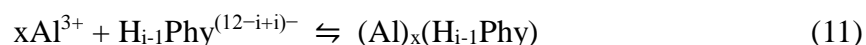
14

suggested that this structure corresponds to MgAlCe-LDHs. Furthermore, the EDS

spectra (Fig. 6) corresponding to zone 1 and zone 2 show that zone 1 is Ce-rich, while

there is no Ce in zone 2. These results may indicated the presence of MgAlCe-LDHs

or/and CeO_2 or/and $Ce(OH)_3$ in zone 1 and the non-uniform distribution of the Ce in

the entire surface. It was worth noting that LDHs were still mainly composed of

MgAl-LDHs in this case.

After intercalating phosphate ions, the surface morphology of *PEO-Ce-LDH-P*

changed, which was attributed to recrystallization [47]. It also has been reported that

this change in morphology is related with the occurrence of fragmentation in the

initial stage of fast anion exchange [48].

Moreover, as suggested by Crea *et al.* [49], PA also can deprotonate according to

the following equilibrium:

$$H_iPhy^{12-i} \leftrightharpoons H^+ + H_{i-1}Phy^{(12-i+1)-} \ (i = 12, 11, \ldots, 2, 1) \tag{10}$$
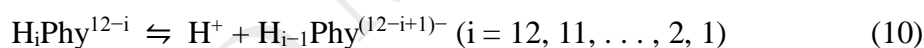
where the completely deprotonated form of PA is denoted by Phy^{12-}. Moreover, it is

worth noting that PA can strongly chelate with metal cations. Mg^{2+} and Al^{3+} from the

Mg substrate or/and Mg and Al oxides/hydroxides chelate with PA and form

deposition products. The chemical reactions are as follows [50]:

$$xAl^{3+} + H_{i-1}Phy^{(12-i+i)-} \leftrightharpoons (Al)_x(H_{i-1}Phy) \tag{11}$$

$$yMg^{2+} + H_{i-1}Phy^{(12-i+i)-} \leftrightharpoons (Mg)_y(H_{i-1}Phy) \tag{12}$$

3.2 Cross-section SEM and GDOES analyses

Fig. 7 shows cross-sectional SEM images of different specimens. Fig. 7a shows

that there were different sized pores throughout the PEO coating. Accordingly, sealing

15

is a necessary step to increase the corrosion resistance of any anodized layer [51].

After the further treatment in the Ce containing solution, the CCC layer shown in Fig.

6b, covered the entire surface of the PEO coating, accompanied by micro-crack

formation. The CCC exhibited a sealing effect on the PEO coating, which is marked

in Fig. 6b. At the beginning of the treatment, the Ce solution penetrated into the pores

of the PEO layer to precipitate of CeO_2 or/and $Ce(OH)_3$. Then these pores were

covered with spherical deposits. The spherical deposits simultaneously formed on the

surface of the PEO layer, creating a barrier to the inward permeation of Ce solution

into underlying pores of PEO layer. After the deposition of the LDHs on *PEO-Ce*, the

thickness and the density of the coating had significantly increased. There was a two-

layer structure as shown in Fig. 7c. According to our previous work, on the one hand,

the LDH coating growth depends strongly on the dissolution of the PEO coating. On

the other hand, the PEO coating cannot be dissolved completely. The inner layer is a

result of the inwards growth of coating, and mainly consisted of $Mg(OH)_2$ and LDHs,

as described above. The outer layer is a mixed layer including Mg, Al and Ce oxides

or hydroxides. Fig. 7d shows a slight increase in thickness to 2.8 μm and that the

coating had become compact.

The GDOES depth profiles for the different specimens are shown in Fig. 8. There

were three main regions in the depth profiles of *PEO* (Fig. 8a): (I) PEO layer

sputtering; (II) sputtering transition from the PEO layer to the substrate; and (III) the

substrate sputtering. For *PEO-Ce* (Fig. 8b), the O signal rapidly increased and then

rapidly decreased and Ce enriched in Zone I. This result indicated the enrichment of

Ce oxides or hydroxides in the surface of *PEO-Ce*, which was consistent with the

SEM cross-sectional image. Zones II, III and IV were the PEO layer sputtering, the

simultaneous sputtering of the PEO layer and the Mg substrate and sputtering of the

Mg substrate, respectively. After fabrication of LDHs on *PEO-Ce* (Fig. 8c), the Mg,

Al, O and Ce signals were similar to *PEO-Ce*. The N signal existed in Zone I and

Zone II, indicating the presence of nitrate-containing LDHs in these two zones. After

the ion-exchange reaction for *PEO-Ce-LDH* (Fig. 8d), the P signal appeared in Zone I

and Zone II, which indicated that PO_4^{3-} was intercalated into the LDH galleries

successfully. Moreover, it was worth noting that Ce signal was also detected in Zone

II (markedly in Fig. 8d), which was significantly different from *PEO-Ce* and *PEO-*

Ce-LDH. This result may indicate to the Ce inward diffusion to the substrate, and this

diffusion may be correlated with the recrystallization or the occurrence of

fragmentation during the HA treatment process

3.3 The overall corrosion resistance

Fig. 9 shows representative polarization curves of different specimens in 3.5 wt.%

NaCl aqueous solution. For comparison, the polarization curve of the Mg substrate is

also shown in Fig. 9. The corrosion parameters are summarized in Table 2, where E_{corr}

and i_{corr} are the corrosion potential and the corrosion current density, respectively, b_c

and b_a are the cathodic and anodic Tafel slopes. The E_{corr} and i_{corr} values for *PEO*

were -0.46 V_{SCE} and 2.31 $\mu A \cdot cm^{-2}$, respectively. In contrast to the Mg substrate, the b_a

and b_c values significantly increased, which implied that the PEO coating hindered

both the anodic reaction and the cathodic reaction. Further treatment in the Ce

17

containing solution, caused the b_c value of *PEO-Ce* to futher increase while b_a

decreased. This result indicated that corrosion products of *PEO-Ce* could block the

cathodic zones, effectively decreasing the cathode area and accordingly suppressing

cathodic hydrogen evolution reaction. As a result, it leaded to a decreasing of current

density ($i_{corr} = 0.68$ µA·cm^{-2}) and a lower corrosion rate. For *PEO-Ce-LDH*, there was

the reverse trend (b_c decreased, b_a increased) compared with *PEO-Ce*. Table 2 shows

a considerable decrease of i_{corr} in *PEO-Ce-LDH-P*; i_{corr} decreased by around 2-3

orders of magnitude when compared to the Mg substrate, which implied the best

corrosion protection for *PEO-Ce-LDH-P*. Moreover, the polarization resistance (R_p),

which is inversely proportional to the corrosion rate, can be calculated using the

simplified Stern-Geary equation [52]:

$$R_p = \frac{b_a \times b_c}{2.3 i_{corr}(b_a + b_c)}$$

The calculated values of R_p are also presented in Table 2. In addition, the two

breakdown potentials (E_{b1} and E_{b2}) for *PEO-Ce-LDH* and *PEO-Ce-LDH-P* can be

ascribed to the self-healing, which is discussed in section 3.4.

Fig. 10 presents Bode plots for different specimens after (a) 30 min, (b) 7 days

and (c) 21 days immersion in 3.5 wt.% NaCl aqueous solution at room temperature.

The EIS spectrum in a broad frequency range may exhibit one, two or more time

constants depending on whether the coating has a single-layered or multi-layered

structure, whether it is porous or compact, whether the space-charge region that puts

restrictions on the charge transfer forms at the potential used, or the charge transfer

process is effected by diffusion [53]. Fig. 10a shows two well-defined time constants

18

in the frequency-phase angle diagram. The relaxation process at high frequencies corresponds to the porous layer, and the other at low frequencies, to the inner compact layer. Usually, the electrochemical properties of the coatings and their specific structural features or physicochemical process are characterized by an equivalent circuit (EC) to interpret the EIS spectrum. The EC in Fig. 10d (i) was used to fit EIS data in Fig. 10a. R_{sol} corresponds to the solution resistance; R_{por} and CPE_{por} are the resistive and capacitive response of the outer porous layer; R_{inn} and CPE_{inn} are the resistive and capacitive response of the inner compact layer. Because of the nonhomogeneity, caused by heterogeneity of chemical composition, the degree of crystallinity and stoichiometry, and the presence of the space-charge region, it was not possible to analyze the interfacial processes of charge transfer using ideal capacitors and resistors [53]. Therefore, the constant phase elements (*CPE*) were used herein to characterize the non-ideal resistive and capacitive behavior of the coated specimens [54], described by the formula:

$$Z(\omega) = \mathrm{K}(j\omega)^{-n},$$

where *n* is the angular frequency, $\mathrm{j} = \sqrt{-1}$, and $0 < n < 1$. Table 3 lists the fitting results. R_{por} of *PEO-Ce* was lower than that of *PEO*, which was attributed to the poor adhesion to the PEO layer. Moreover, the values of n_{inn} of *PEO* and *PEO-Ce* were close to 1, which indicated a capacitive behavior with excellent dielectric properties.

After 7 days and 21 days in contact with the 3.5 wt.% NaCl aqueous solution, the relaxation processes in some cases were difficult to distinguish in Fig. 10b and 10c due to a strong overlap. But the chi-squared (χ^2) error value was 10^{-3} order of

19

magnitude for all cases, implying that the EC in Fig. 10d (ii) was adequate for fitting

Fig. 10b and 10c. When the aggressive media reach the coating/metal interface

through micro-pores or micro-cracks, the corrosion of Mg substrate begin to occur.

The corrosion process can be interpreted by the capacitive response of the double

layer on the electrolyte/substrate interface (CPE_{dl}) and the Faradaic charge transfer

resistance (R_{ct}), which is associated with the electrochemical reactions in the

electrolyte/substrate interface region. After immersion of 7 days, both R_{por} and R_{inn} of

all specimens increased, indicating a significant improvement of the coating

protective properties. Especially, *PEO-Ce-LDH* had the highest values in R_{por}

($4.3 \times 10^5 \, \Omega \, cm^2$) and R_{inn} ($1.6 \times 10^6 \, \Omega \, cm^2$) compared with others. After further

immersion to 21 days, *PEO*, *PEO-Ce* and *PEO-Ce-LDH* in R_{por}, R_{inn} and R_{ct} began to

decrease in different degrees. Nevertheless, R_{por}, R_{inn} and R_{ct} of *PEO-Ce-LDH-P* all

exhibited an increasing trend, which indicated a superior self-healing ability for the

defects in the corrosion process. Usually, the low-frequency impedance modulus

($|Z|_{0.01 \, Hz}$) also exhibits the overall protective performance of the coating [29]. Table 3

shows that R_{ct} of $4.3 \times 10^9 \, \Omega \, cm^2$ for *PEO-Ce-LDH-P* was four orders of magnitude

larger than that of *PEO-Ce-LDH* ($3.3 \times 10^5 \, \Omega \, cm^2$), indicating a good synergistic effect

between Ce species and PO_4^{3-} ions in the corrosion protection.

Fig. 11 shows the XRD patterns and corresponding optical photographs (the

inserts) after 21 days immersion in 3.5 wt.% NaCl aqueous solution. For *PEO* and

PEO-Ce, diffraction peaks corresponding to $Mg(OH)_2$ were significantly larger than

for the other coatings, indicating their corrosion products were mainly $Mg(OH)_2$ and

20

consistent with considerable corrosion during the immersion. The inserts show that

PEO and *PEO-Ce* specimens had corroded seriously and were covered with a

significant layer of corrosion products. In contrast, the diffraction peaks for $Mg(OH)_2$

for *PEO-Ce-LDH* and *PEO-Ce-LDH-P* were very weak, indicating a better corrosion

protection of these coatings. The photographs after 21 days of immersion show that

there was corrosion only at the edges of *PEO-Ce-LDH*, whereas there was no obvious

corrosion for *PEO-Ce-LDH-P*.

3.4 Self-healing ability

EIS spectrum gives the averaged global electrochemical response of the

specimens. In contrast, a localized technique such as SVET can provide the localized

electrochemical behavior, including the magnitude and distribution of the anodic and

cathodic activity on the corroding surface [55]. In order to evaluate the self-healing

ability for different specimens, artificial defects were introduced into the coated

specimens by a sharp knife. Fig. 12 presents the optical photographs of the scratches

before the test, and the SVET maps after 2 h, 10 h, and 24 h immersion in 3.5 wt.%

NaCl aqueous solution for the various specimens. The SVET map for *PEO* showed

strong corrosion activity already at the initial stages of immersion, and that the

corrosion intensity did not weaken with longer immersion, indicating that the PEO

coating provides only a barrier protection for the Mg substrate. For *PEO-Ce*, there

were several anodic regions (red colour) and cathodic regions (blue colour) at the

early stages of immersion. With longer immersion, there was a decrease in the

corrosion activity, but, some significant corrosion activities remained and did not fully

disappear. These corrosion activities were marked by red or blue circles. This

indicated that the self-sealing ability of *PEO-Ce* was limited. For LDHs deposited on

PEO-Ce, some electrochemical corrosion activities marked by red or blue circles at

the initial stages decreased remarkably after 24 h immersion. This behavior showed

that the LDHs had the ability to entrap corrosive species (Cl$^-$) as discussed in our

previous study [19]. Some level of corrosion retardation was also the result of the

release of Ce from the coating. The released Ce cations precipitated in the cathodic

areas to heal these scratches.

As for *PEO-Ce-LDH-P*, several anodic and cathodic regions marked in Fig. 12

also showed a decrease after 24 h exposure to NaCl solution. Combined with the front

view and left view of the SVET map (Fig. 13), it is indicated that the best corrosion

protection and self-healing performance occurred for *PEO-Ce-LDH-P*. The good

inhibitive action of *PEO-Ce-LDH-P* can be ascribed to the release of inhibitive

species (PO$_4^{3-}$) from the LDH and the precipitation on the anodic regions of

Mg$_3$(PO$_4$)$_2$. The synergistic effect between the Ce cations released from the coating

with PO$_4^{3-}$ anions leads to better coating formation on the scratch with higher

inhibition performance. Moreover, this synergistic effect is favored by the Ce inward

diffusion during HA treatment (Fig. 8). Fig. 14 shows the surface topographies around

the artificial defects after 24 h immersion for different specimens. The artificial defect

in *PEO* was mainly covered by the corrosion product Mg(OH)$_2$, and only exhibited a

passive corrosion protection. Fig. 14c (*PEO-Ce-LDH*) shows that some local regions

had not been healed well. The best self-healing ability was for *PEO-Ce-LDH-P*,

where the compact insoluble precipitate covered the entire defect. These results were in good agreement with the SVET results.

In summary, PEO layer only provides a passive corrosion protection for substrates. The PEO specimens treated by Ce show a limited active corrosion protection. Matter *et al.* [56] suggested Ce(III) revealed a better inhibitive ability than Ce(IV) at relatively similar conditions of concentration and exposure time. In addition, PEO specimens treated by Ce and LDHs and then loaded with PA exhibit a strong self-healing ability.

4. Conclusion

(1) Ce in *PEO-Ce* mainly existed in the 4-valence state as CeO_2 (79%) with some in the 3-valence state as $Ce(OH)_3$ (21%). After deposition of LDHs on the *PEO-Ce*, the content of CeO_2 decreased to 59% in *PEO-Ce-LDH* and 61% in *PEO-Ce-LDH-P* respectively. This can be attributed to i) more $Ce(OH)_3$ formation and ii) a small amount of Ce^{3+} may have diffused into the LDHs layers resulting in the formation of MgAlCe-LDHs.

(2) The surface of *PEO-Ce* was covered with cerium-rich nodules. *PEO-Ce-LDH* showed two different surface morphologies, namely a flake-like structure and circular or hexagonal platelet-like structure corresponding to the Ce-rich zones and Ce-free zones respectively. The result also indicated the non-uniform distribution of the Ce in the entire surface. Moreover, production of the MgAl-LDH coating on the *PEO-Ce* specimens leaded to an increasing in coating thickness.

23

(3) PEO layer only provided a passive corrosion protection for substrates. After the Ce treatment there was a limited active corrosion protection. Because of the synergistic effect between Ce species and phosphate, the best self-healing ability was for *PEO-Ce-LDH-P*, where the compact insoluble precipitate covered the entire defect. Furthermore, *PEO-Ce-LDH-P* exhibited a good corrosion protection, better than other coatings.

Acknowledgements

References

[1] A. Atrens, G.-L. Song, M. Liu, Z. Shi, F. Cao, M.S. Dargusch, Review of Recent Developments in the Field of Magnesium Corrosion, Adv. Eng. Mater. 17 (2015) 400-453.

[2] Gh. Barati Darband, M. Aliofkhazraei, P. Hamghalam, N. Valizade, Plasma electrolytic oxidation of magnesium and its alloys: Mechanism, properties and applications, J. Magnesium Alloys 5 (2017) 74-132.

[3] A.E. Hughes, J.M.C. Mol, M.L. Zheludkevich, R.G. Buchheit, Introduction, First ed., Active proctive coatings, Melbourne, 2016.

[4] X. Jiang, R. Guo, S. Jiang, Evaluation of self-healing ability of Ce–V conversion coating on AZ31 magnesium alloy, J. Magnesium Alloys 4 (2016) 230-241.

[5] S.R. White, N.R. Sottos, P.H. Geubelle, J.S. Moore, M.R. Kessler, S.R. Sriram, E.N. Brown, S. Viswanathan, Autonomic healing of polymer composites, Lett. Nat. 409 (2001) 794-797.

[6] K. Zhang, L. Wang, G. Liu, Copper(II) 8-hydroxyquinolinate 3D network film with corrosion inhibitor embedded for self-healing corrosion protection, Corros. Sci. 75 (2013) 38-46.

[7] D.G. Shchukin, M. Zheludkevich, K. Yasakau, S. Lamaka, M.G.S. Ferreira, H. Möhwald, Layer-by-Layer Assembled Nanocontainers for Self-Healing Corrosion Protection, Adv. Mater. 18 (2006) 1672-1678.

[8] D.O. Grigoriev, T. Bukreeva, H. Möhwald, D.G. Shchukin, New method for fabrication of loaded micro- and nanocontainers: emulsion encapsulation by

polyelectrolyte layer-by-layer deposition on the liquid core, Langmuir 24 (2008) 999–1004.

[9] Q. Dong, Z. Ba, Y. Jia, Y. Chen, X. Lv, X. Zhang, Z. Wang, Effect of solution concentration on sealing treatment of Mg-Al hydrotalcite film on AZ91D Mg alloy, J. Magnesium Alloys 5 (2017) 320-325.

[10] J. Chen, Y. Song, D. Shan, E.-H. Han, Modifications of the hydrotalcite film on AZ31 Mg alloy by phytic acid: The effects on morphology, composition and corrosion resistance, Corros. Sci. 74 (2013) 130-138.

[11] L. Wu, D. Yang, G. Zhang, Z. Zhang, S. Zhang, A. Tang, F. Pan, Fabrication and characterization of Mg-M layered double hydroxide films on anodized magnesium alloy AZ31, Appl. Surf. Sci. 431 (2018), 177-186.

[12] M.L. Zheludkevich, S.K. Poznyak, L.M. Rodrigues, D. Raps, T. Hack, L.F. Dick, T. Nunes, M.G.S. Ferreira, Active protection coatings with layered double hydroxide nanocontainers of corrosion inhibitor, Corros. Sci. 52 (2010) 602-611.

[13] G. Zhang, L. Wu, A. Tang, B. Weng, A. Atrens, S. Ma, L. Liu, F. Pan, Sealing of anodized magnesium alloy AZ31 with MgAl layered double hydroxides layers, RSC Adv. 8 (2018) 2248-2259.

[14] J. Tedim, A. Kuznetsova, A.N. Salak, F. Montemor, D. Snihirova, M. Pilz, M.L. Zheludkevich, M.G.S. Ferreira, Zn–Al layered double hydroxides as chloride nanotraps in active protective coatings, Corros. Sci. 55 (2012) 1-4.

[15] M.L. Zheludkevich, J. Tedim, M.G.S. Ferreira, "Smart" coatings for active corrosion protection based on multi-functional micro and nanocontainers,

Electrochim. Acta 82 (2012) 314-323.

[16] B. Dou, Y. Wang, T. Zhang, B. Liu, Y. Shao, G. Meng, F. Wang, Growth Behaviors of Layered Double Hydroxide on Microarc Oxidation Film and Anti-Corrosion Performances of the Composite Film, J. Electrochem. Soc. 163 (2016) C917-C927.

[17] M. Serdechnova, A.N. Salak, F.S. Barbosa, D.E.L. Vieira, J. Tedim, M.L. Zheludkevich, M.G.S. Ferreira, Interlayer intercalation and arrangement of 2-mercaptobenzothiazolate and 1,2,3-benzotriazolate anions in layered double hydroxides: In situ X-ray diffraction study, J. Solid State Chem. 233 (2016) 158-165.

[18] M. Mohedano, M. Serdechnova, M. Starykevich, S. Karpushenkov, A.C. Bouali, M.G.S. Ferreira, M.L. Zheludkevich, Active protective PEO coatings on AA2024: Role of voltage on in-situ LDH growth, Mater. Des. 120 (2017) 36-46.

[19] G. Zhang, L. Wu, A. Tang, S. Zhang, B. Yuan, Z. Zheng, F. Pan, A Novel Approach to Fabricate Protective Layered Double Hydroxide Films on the Surface of Anodized Mg-Al Alloy, Adv. Mater. Interfaces 4 (2017) 1700163.

[20] L. Wu, G. Zhang, A. Tang, Y. Liu, A. Atrens, F. Pan, Communication—Fabrication of Protective Layered Double Hydroxide Films by Conversion of Anodic Films on Magnesium Alloy, J. Electrochem. Soc. 164 (2017) C339-C341.

[21] B. Valdez, S. Kiyota, M. Stoytcheva, R. Zlatev, J.M. Bastidas, Cerium-based conversion coatings to improve the corrosion resistance of aluminium alloy 6061-T6, Corros. Sci. 87 (2014) 141-149.

[22] M. Mohedano, C. Blawert, M.L. Zheludkevich, Cerium-based sealing of PEO

coated AM50 magnesium alloy, Surf. Coat. Technol. 269 (2015) 145–154.

[23] M. Laleh, F. Kargar, A.S. Rouhaghdam, Investigation of rare earth sealing of porous micro-arc oxidation coating formed on AZ91D magnesium alloy, J. Rare Earths 30 (2012) 1293-1297.

[24] X.B. Chen, N. Birbilis, T.B. Abbott, Review of corrosion-resistant conversion coatings for magnesium and its alloys, Corros. 67 (2011) 1-16.

[25] F.H. Scholes, C. Soste, A.E. Hughes, S.G. Hardin, P.R. Curtis, The role of hydrogen peroxide in the deposition of cerium-based conversion coatings, Appl. Surf. Sci. 253 (2006) 1770-1780.

[26] L. Wu, D. Yang, G. Zhang, Z. Zhang, S. Zhang, A. Tang, F. Pan, Fabrication and characterization of Mg-M layered double hydroxide films on anodized magnesium alloy AZ31, Appl. Surf. Sci. 431 (2017) 177

[27] K.H. Goh, T.T. Lim, Z. Dong, Application of layered double hydroxides for removal of oxyanions: a review, Water Res. 42 (2008) 1343-1368.

[28] Y. Wang, W. Peng, L. Liu, F. Gao, M. Li, The electrochemical determination of l-cysteine at a Ce-doped Mg–Al layered double hydroxide modified glassy carbon electrode, Electrochim. Acta 70 (2012) 193-198.

[29] Y. Zhang, Y. Li, Y. Ren, H. Wang, F. Chen, Double-doped LDH films on aluminum alloys for active protection, Mater. Lett. 192 (2017) 33-35.

[30] M. Serdechnova, M. Mohedano, B. Kuznetsov, C.L. Mendis, M. Starykevich, S. Karpushenkov, J. Tedim, M.G.S. Ferreira, C. Blawert, M.L. Zheludkevich, PEO Coatings with Active Protection Based on In-Situ Formed LDH-Nanocontainers, J.

Electrochem. Soc. 164 (2017) C36-C45.

[31] J. Carneiro, A.F. Caetano, A. Kuznetsova, F. Maia, A.N. Salak, J. Tedim, N. Scharnagl, M.L. Zheludkevich, M.G.S. Ferreira, Polyelectrolyte-modified layered double hydroxide nanocontainers as vehicles for combined inhibitors, RSC Adv. 5 (2015) 39916-39929.

[32] E. Bêche, P. Charvin, D. Perarnau, S. Abanades, G. Flamant, Ce 3d XPS investigation of cerium oxides and mixed cerium oxide (CexTiyOz), Surf. Interface Anal. 40 (2008) 264-267.

[33] B.F. Rivera, B.Y. Johnson, M.J. O'Keefe, W.G. Fahrenholtz, Deposition and characterization of cerium oxide conversion coatings on aluminum alloy 7075-T6, Surf. Coat. Technol. 176 (2004) 349-356.

[34] J. Światowska, V. Lair, C. Pereira-Nabais, G. Cote, P. Marcus, A. Chagnes, XPS, XRD and SEM characterization of a thin ceria layer deposited onto graphite electrode for application in lithium-ion batteries, Appl. Surf. Sci. 257 (2011) 9110-9119.

[35] X. Yu, G. Li, XPS study of cerium conversion coating on the anodized 2024 aluminum alloy, J. Alloys Compd. 364 (2004) 193-198.

[36] A.P. Loperena, I.L. Lehr, S.B. Saidman, Formation of a cerium conversion coating on magnesium alloy using ascorbic acid as additive. Characterisation and anticorrosive properties of the formed films, J. Magnesium Alloys 4 (2016) 278-285.

[37] R. Leppelt, B. Schumacher, V. Plzak, M. Kinne, R. Behm, Kinetics and mechanism of the low-temperature water–gas shift reaction on Au/CeO2 catalysts in an idealized reaction atmosphere, J. Catal. 244 (2006) 137-152.

[38] C. Ke, Y. Wu, Y. Qiu, J. Duan, N. Birbilis, X.-B. Chen, Influence of surface chemistry on the formation of crystalline hydroxide coatings on Mg alloys in liquid water and steam systems, Corros. Sci. 113 (2016) 145-159.

[39] B.S. Liu, Y.F. Kuang, Y.S. Chai, D.Q. Fang, M.G. Zhang, Y.H. Wei, Degradation research of protective coating on AZ91D Mg alloy components via simulated contamination, J. Magnesium Alloys 4 (2016) 220-229.

[40] E. Alibakhshi, E. Ghasemi, M. Mahdavian, B. Ramezanzadeh, A comparative study on corrosion inhibitive effect of nitrate and phosphate intercalated Zn-Al-layered double hydroxides (LDHs) nanocontainers incorporated into a hybrid silane layer and their effect on cathodic delamination of epoxy topcoat, Corros. Sci. 115 (2017) 159-174.

[41] F. Zhang, C. Zhang, R. Zeng, L. Song, L. Guo, X. Huang, Corrosion Resistance of the Superhydrophobic Mg(OH)2/Mg-Al Layered Double Hydroxide Coatings on Magnesium Alloys, Met. 6 (2016) 85.

[42] Y. Zhang, P. Yu, Y. Qi, F. Chen, Y. Li, Y. Zhang, Oleylamine/graphene-modified hydrotalcite-based film on titanium alloys and its lubricating properties, Mater. Lett. 193 (2017) 93-96.

[43] E. Alibakhshi, E. Ghasemi, M. Mahdavian, B. Ramezanzadeh, S. Farashi, Fabrication and Characterization of PO_4^{3-} Intercalated Zn-Al- Layered Double Hydroxide Nanocontainer, J. Electrochem. Soc. 163 (2016) C495-C505.

[44] S.S. Farhadi, M. Aliofkhazraei, Gh. Barati Darband, A. Abolhasani, A. Sabour Rouhaghdam, Corrosion and wettability of PEO coatings on magnesium by addition

of potassium stearate, J. Magnesium Alloys 5 (2017) 210-216.

[45] M. Mohedano, C. Blawert, M.L. Zheludkevich, Silicate-based Plasma Electrolytic Oxidation (PEO) coatings with incorporated CeO_2 particles on AM50 magnesium alloy, Mater. Des. 86 (2015) 735-744.

[46] J. Hu, S. Tang, Z. Zhang, Microstructure and formation mechanism of cerium conversion coating on alumina borate whisker-reinforced AA6061 composite, Corros. Sci. 50 (2008) 3185-3192.

[47] Y. Li, S. Li, Y. Zhang, M. Yu, J. Liu, Enhanced protective Zn–Al layered double hydroxide film fabricated on anodized 2198 aluminum alloy, J. Alloys Compd. 630 (2015) 29-36.

[48] A.N. Salak, J. Tedim, A.I. Kuznetsova, M.L. Zheludkevich, M.G.S. Ferreira, Anion exchange in Zn–Al layered double hydroxides: In situ X-ray diffraction study, Chem. Phys. Lett. 495 (2010) 73-76.

[49] F. Crea, C. De Stefano, D. Milea, S. Sammartano, Formation and stability of phytate complexes in solution, Coord. Chem. Rev. 252 (2008) 1108-1120.

[50] H. Shi, E.-H. Han, F. Liu, S. Kallip, Protection of 2024-T3 aluminium alloy by corrosion resistant phytic acid conversion coating, Appl. Surf. Sci. 280 (2013) 325-331.

[51] C. Blawert, W. Dietzel, E. Ghali, G. Song, Anodizing Treatments for Magnesium Alloys and Their Effect on Corrosion Resistance in Various Environments, Adv. Eng. Mater. 8 (2006) 511-533.

[52] L.-Y. Cui, R.-C. Zeng, S.-K. Guan, W.-C. Qi, F. Zhang, S.-Q. Li, E.-H. Han,

Degradation mechanism of micro-arc oxidation coatings on biodegradable Mg-Ca alloys: The influence of porosity, J. Alloys Compd. 695 (2017) 2464-2476.

[53] S.V. Gnedenkov, S.L. Sinebryukhov, V.I. Sergienko, Electrochemical impedance simulation of a metal oxide heterostructure/electrolyte interface: A review, Russ. J. Electrochem. 42 (2006) 197-211.

[54] L. Li, N.D. Nam, Effect of yttrium on corrosion behavior of extruded AZ61 Mg alloy, J. Magnesium Alloys 4 (2016) 44-51.

[55] J. Tedim, A.C. Bastos, S. Kallip, M.L. Zheludkevich, M.G.S. Ferreira, Corrosion protection of AA2024-T3 by LDH conversion films. Analysis of SVET results, Electrochim. Acta 210 (2016) 215-224.

[56] E. A. Matter, S. Kozhukharov, M. Machkova, V. Kozhukharov, Comparison between the inhibition efficiencies of Ce(III) and Ce(IV) ammonium nitrates against corrosion of AA2024 aluminum alloy in solutions of low chloride concentration, Corros. Sci. 62 (2012) 22-33.

Figure captions:

Fig. 1 The schematic representation of the entrapment of the aggressive chloride ions

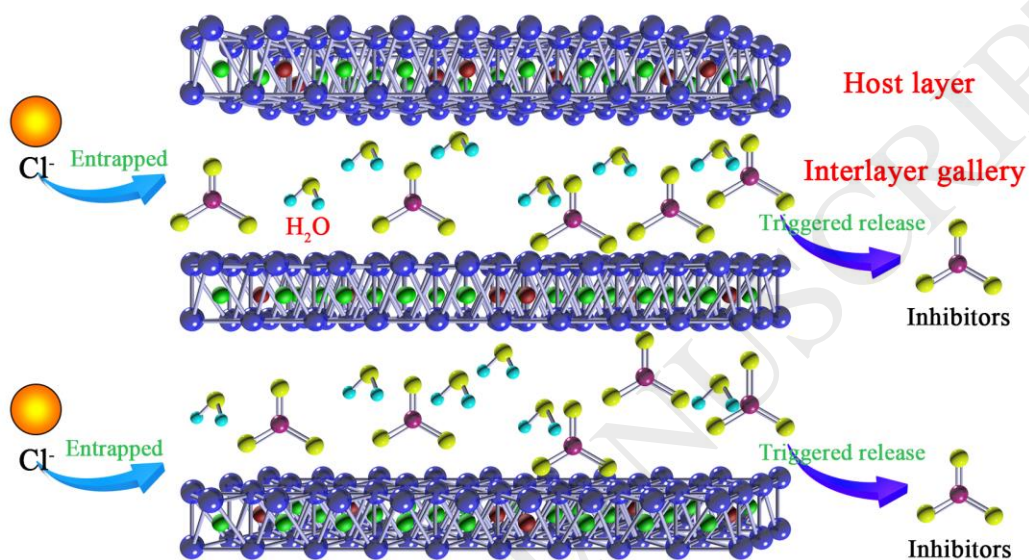and the triggered release of anionic corrosion inhibitors from LDHs.

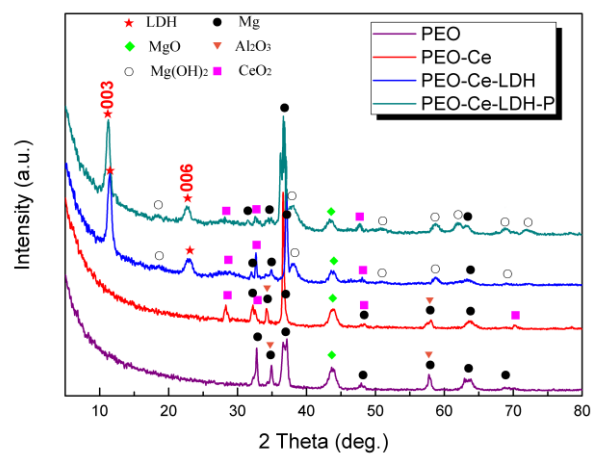Fig. 2 XRD patterns of the different coatings.

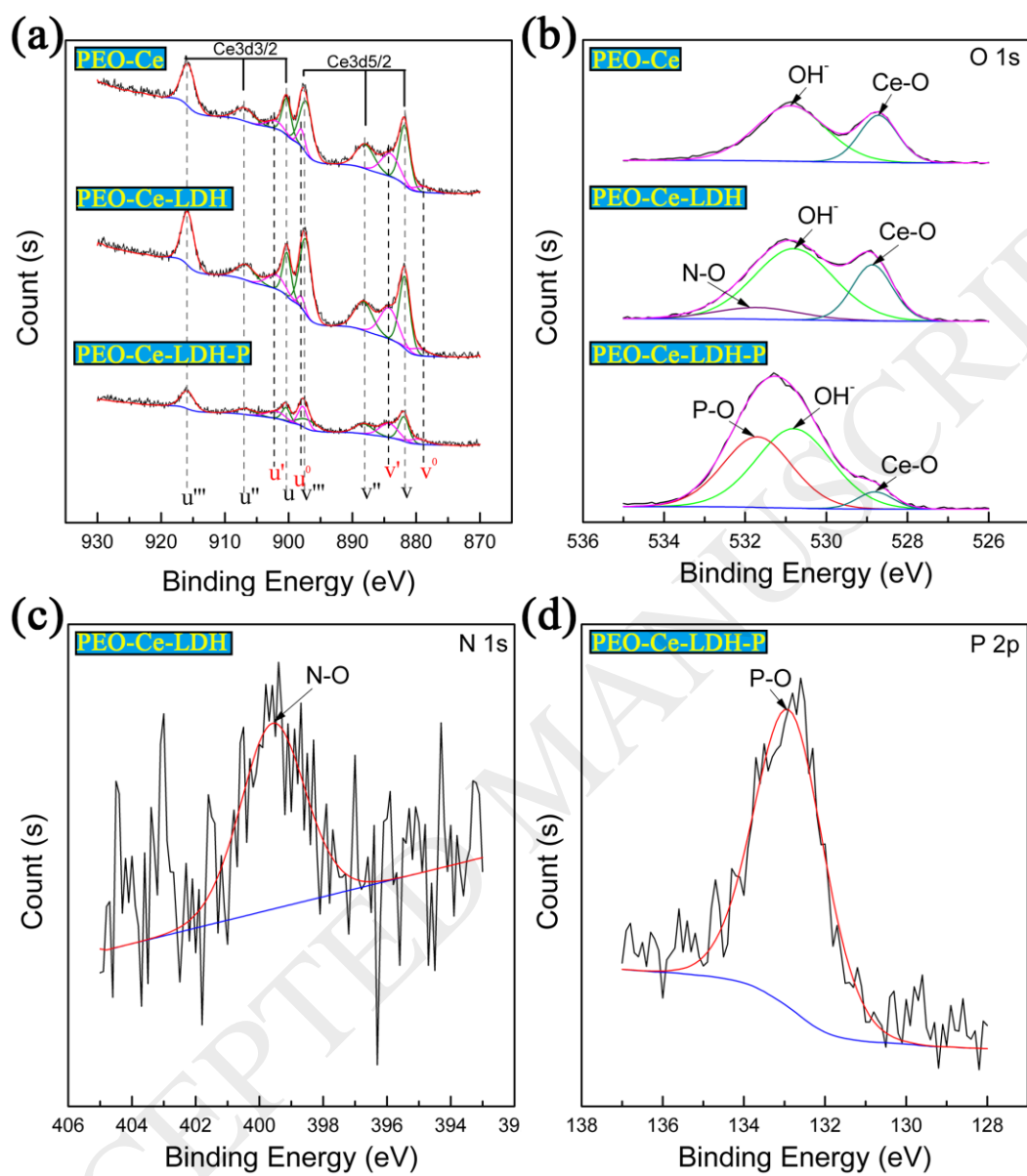Fig. 3 High resolution XPS of (a) Ce 3d; (b) O 1s; (c) N 1s and (d) P 2p.

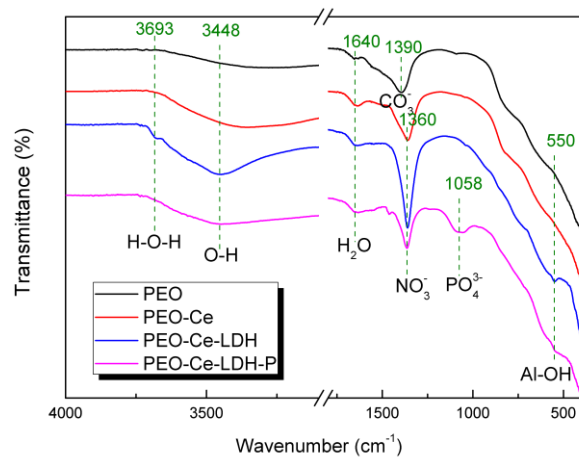Fig. 4 FT-IR spectra for the various coatings.

Fig. 5 SEM micrographs of (a, b) *PEO*; (c, d) *PEO-Ce*; (e, f, g) *PEO-Ce-LDH* and (h,
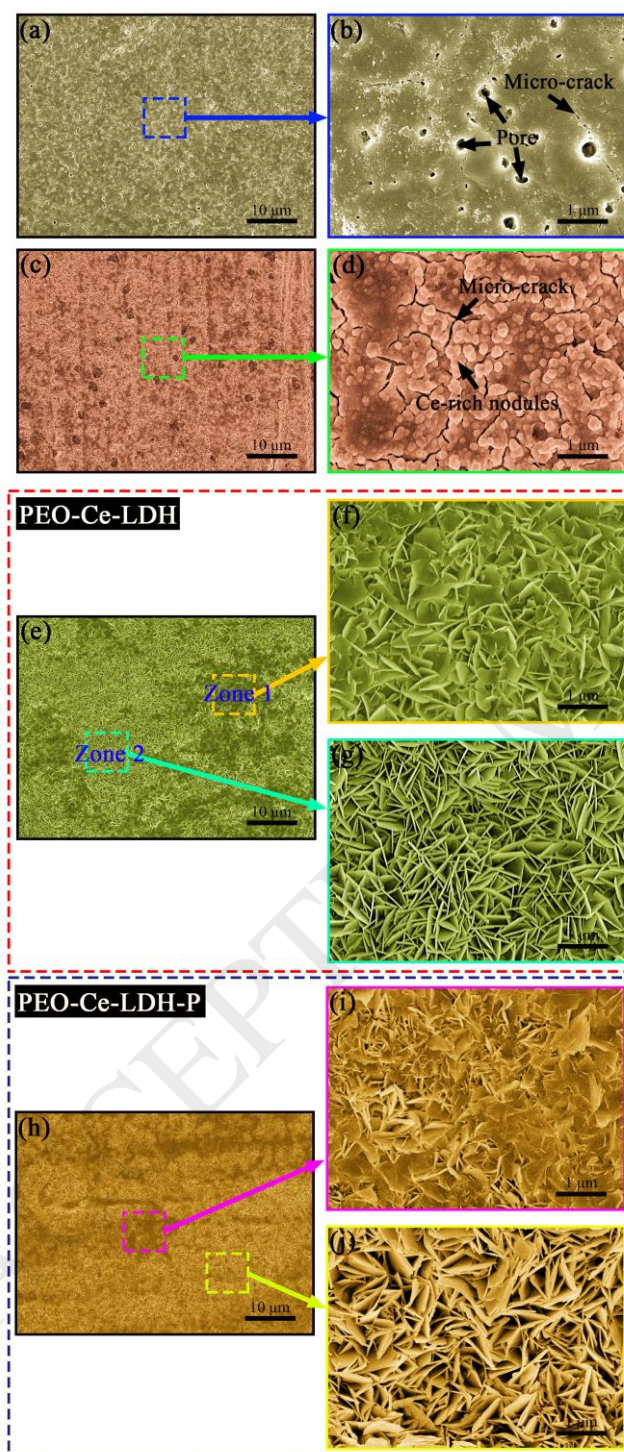
i, j) *PEO-Ce-LDH-P*.

Fig. 6 EDS spectra of (a) zone (I) and (b) zone (II) in Fig. 5e.

(a)

Element	Element content/ at.%
Mg	12
Al	6
Ce	16.7
O	65.2

(b)

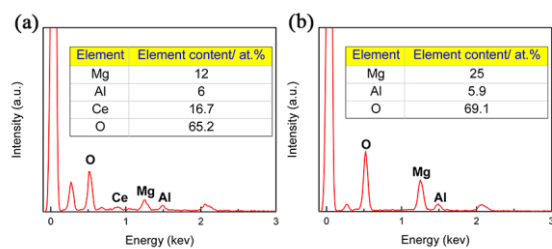| Element	Element content/ at.%
Mg	25
Al	5.9
O	69.1

Fig. 7 Cross-sectional SEM micrographs of (a) *PEO*; (b) *PEO-Ce*; (c) *PEO-Ce-LDH*
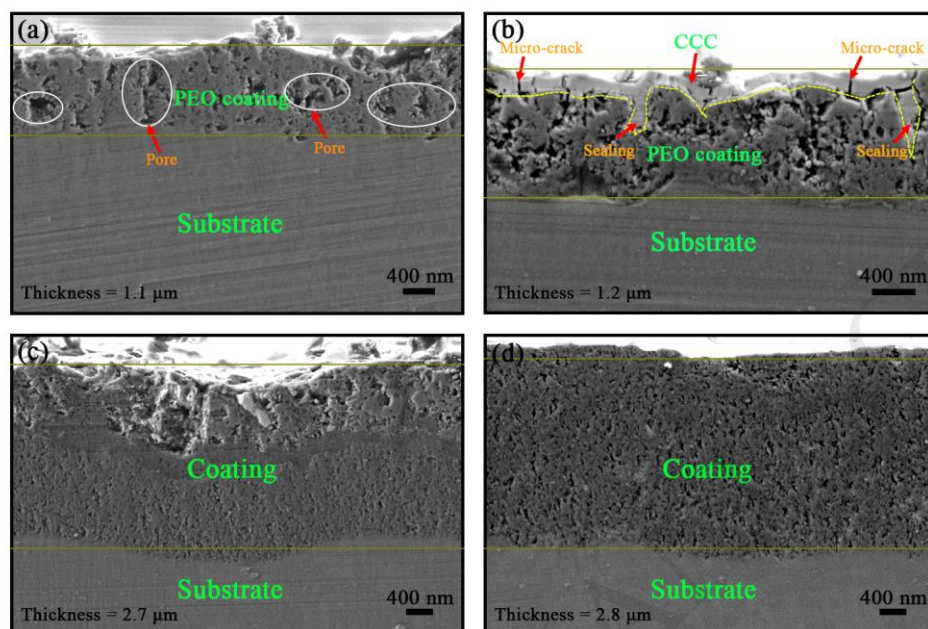
and (d) *PEO-Ce-LDH-P*.

Fig. 8 GDOES depth elemental profiles of (a) *PEO*; (b) *PEO-Ce*; (c) *PEO-Ce-LDH* and (d) *PEO-Ce-LDH-P*.

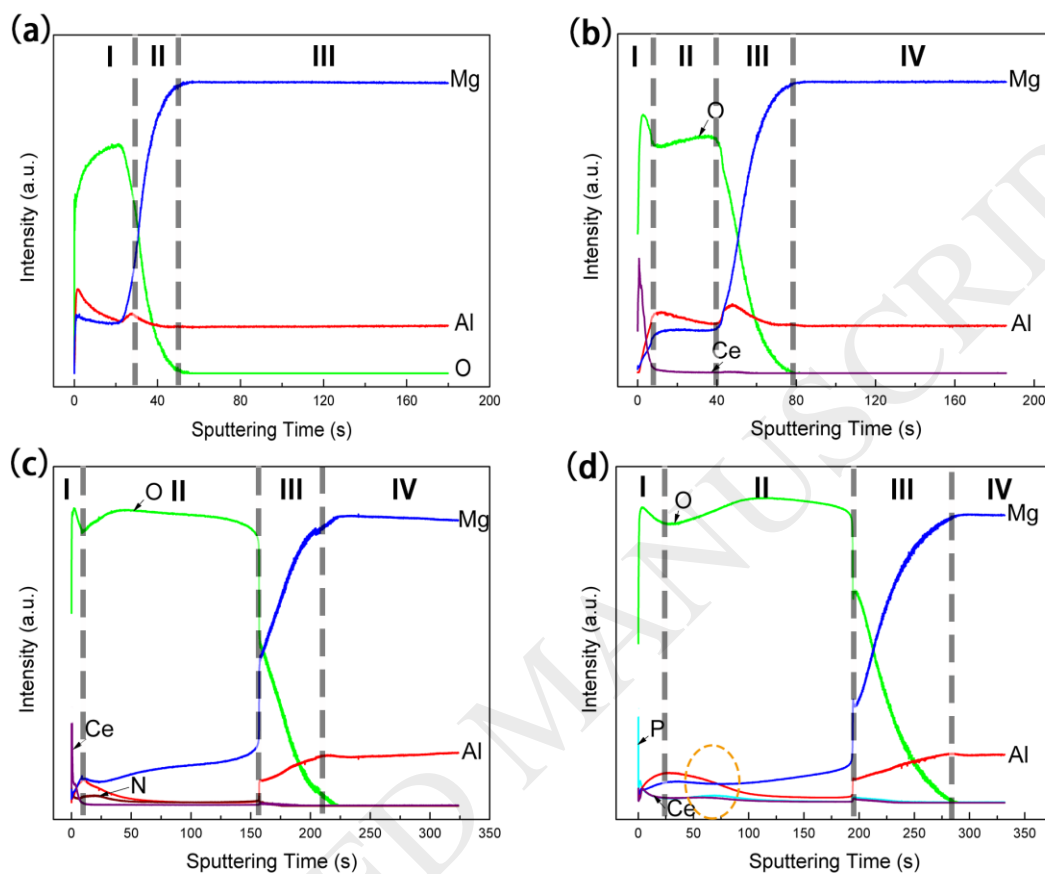Fig. 9 Polarisation potentiodynamic curves measured in 3.5 wt.% NaCl solution for

different specimens.
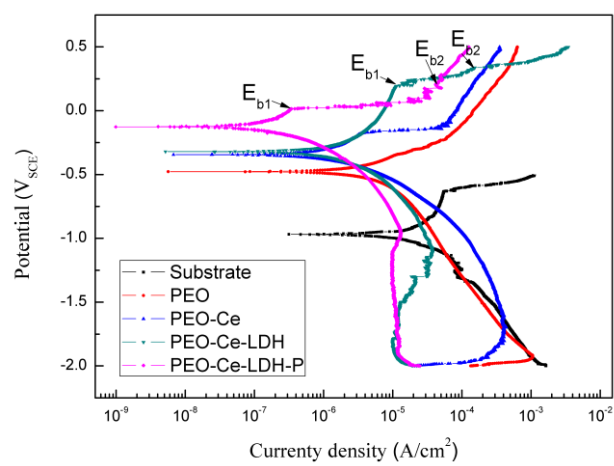
Fig. 10 Impedance spectra obtained for various specimens after (a) 30 min; (b) 7 days and (c) 21 days immersion in 3.5 wt.% NaCl solution. (d) Equivalent circuits used to fit the EIS spectra.
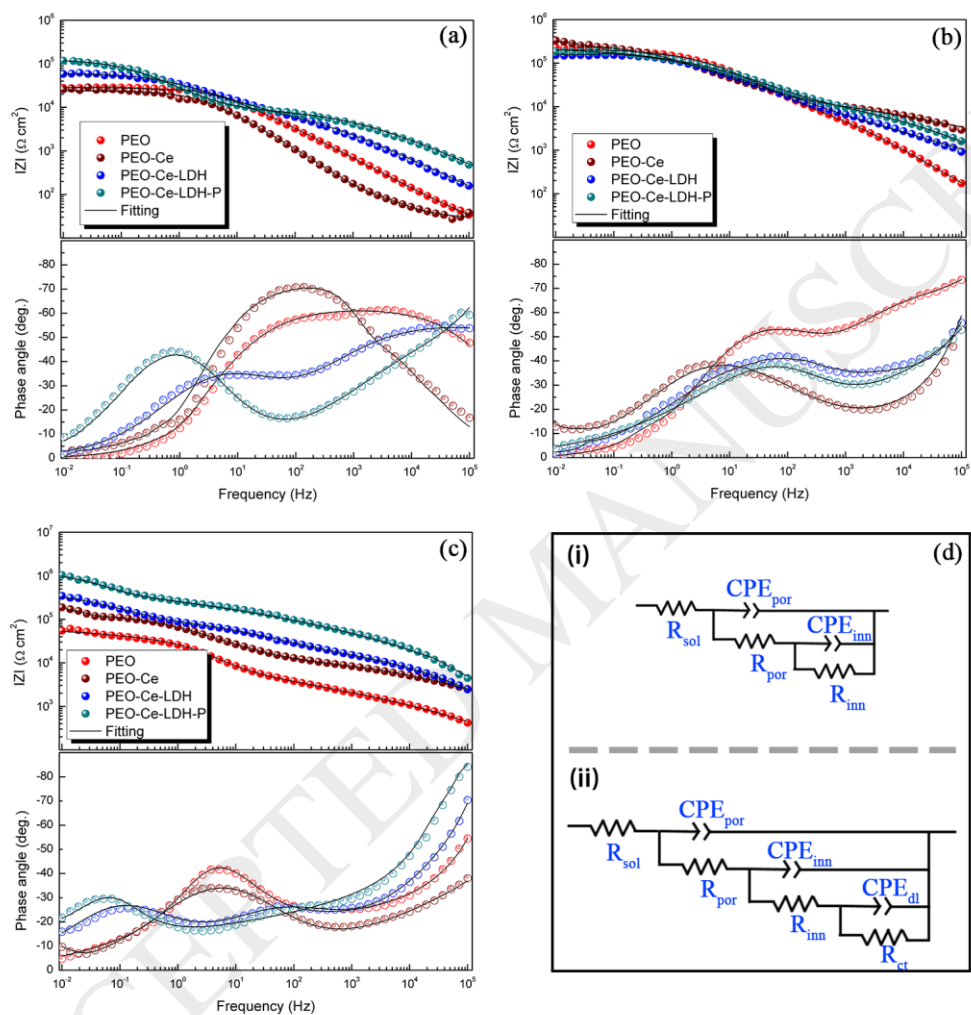
Fig. 11 XRD patterns and photographs of the various specimens after 21 days

immersion in 3.5 wt.% NaCl solution.
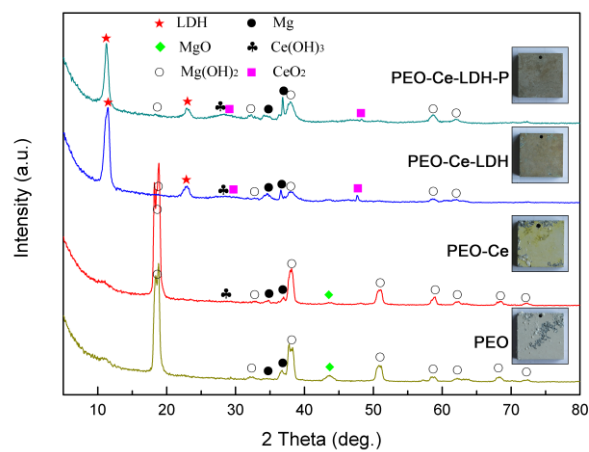
Fig. 12 Microphotographs before immersion in 3.5 wt.% NaCl and SVET maps after immersion in 3.5 wt.% NaCl after 2 h, 10 h, and 24 h for different specimens.

Fig. 13 The front view and left view of SVET maps for different specimens.

Fig. 14 Microphotographs after 24 h immersion in 3.5 wt.% NaCl for (a, A) *PEO*; (b, B) *PEO-Ce*; (c, C) *PEO-Ce-LDH* and (d, D) *PEO-Ce-LDH-P*.

Table 1 Compilation of the data from the Ce 3d XP spectrum, binding energies (B.

E.), peak area ratio and the content of Ce (III) and Ce (IV).

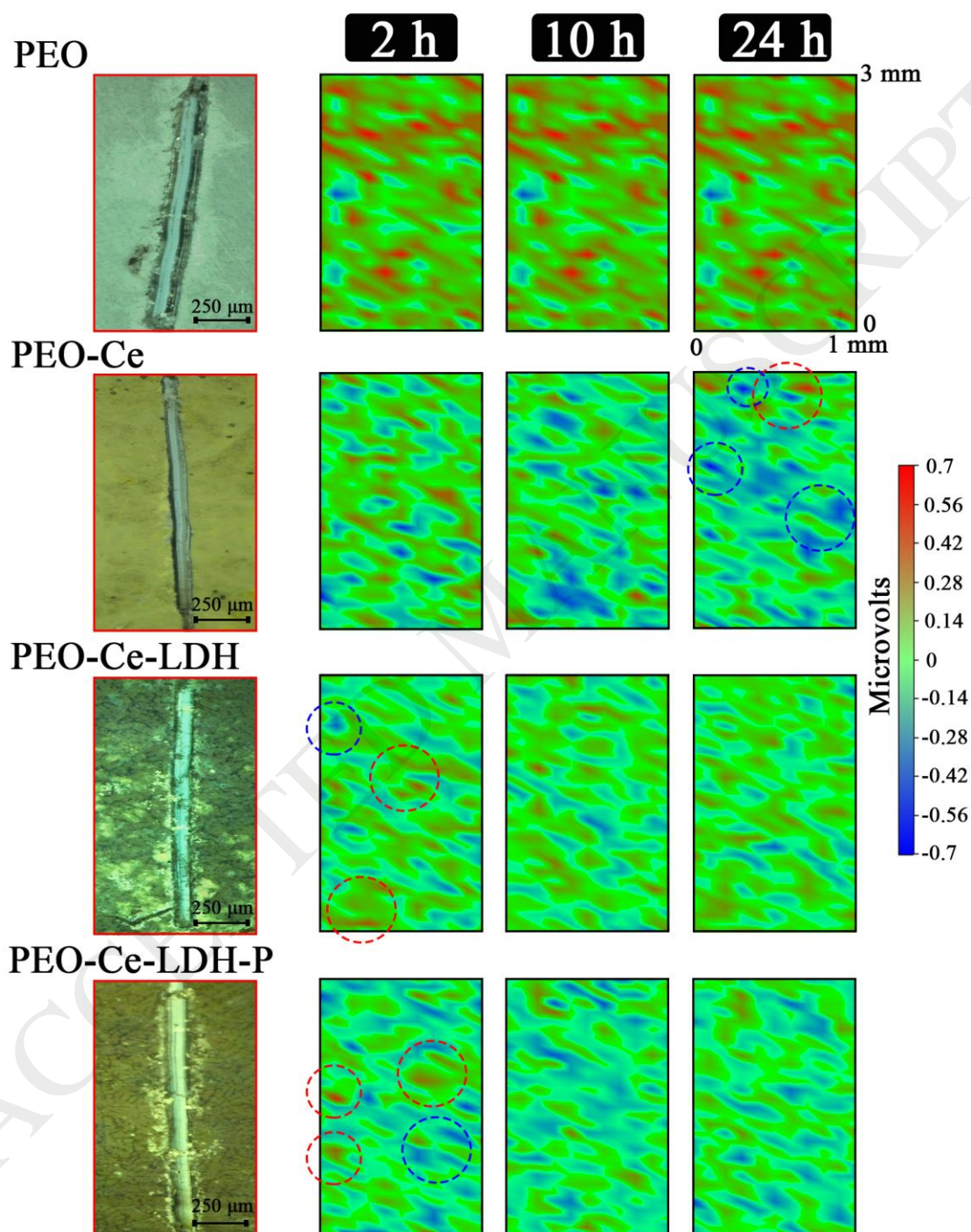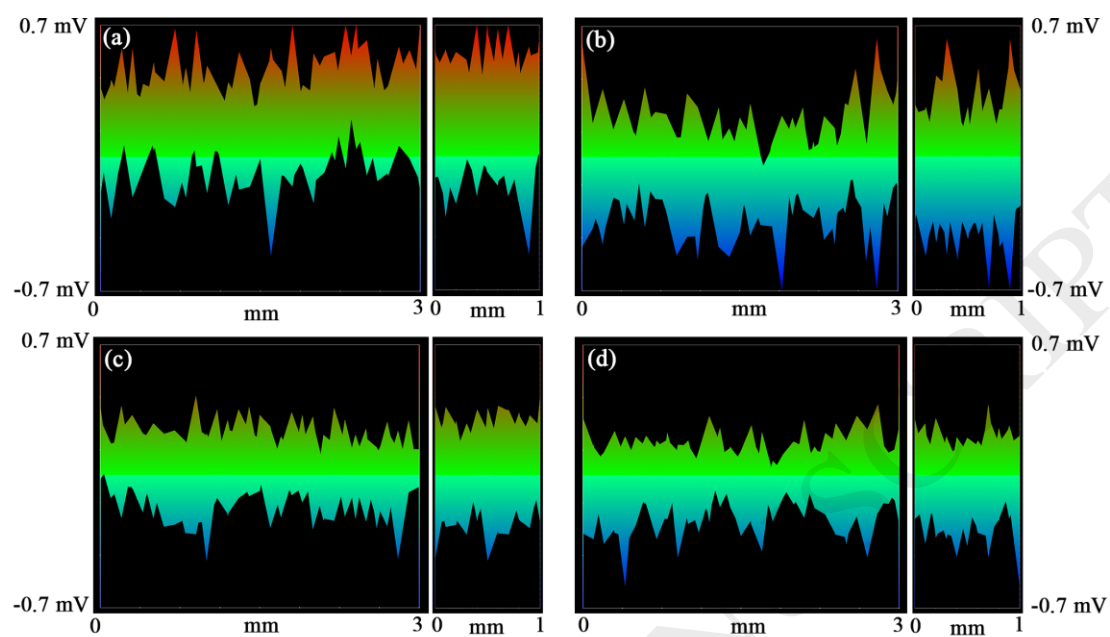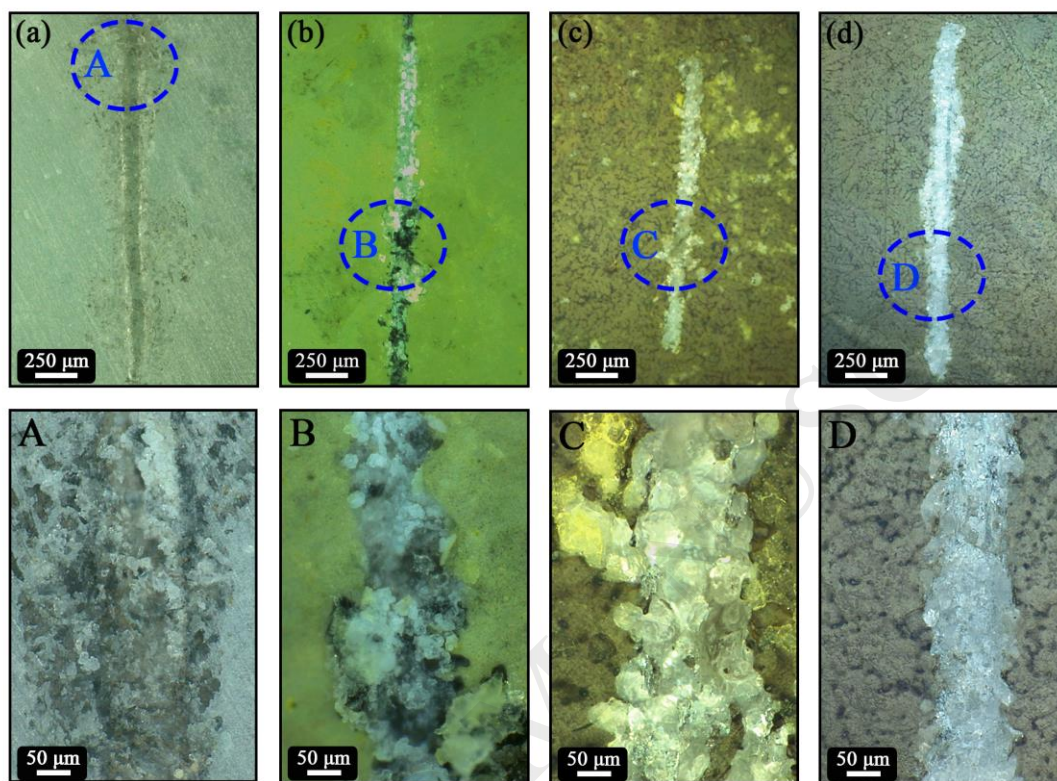|		Ce (III)					Ce (IV)					
		v^0	v'	u^0	u'		v	v''	v'''	u	u''	u'''
PEO-Ce	B. E.	878.9	884.1	898.0	902.1		881.8	888.0	897.3	900.3	906.9	916.1
	Area ratio	0.16	0.63	0.19	0.19		0.96	0.67	1	0.49	0.36	0.90
	Content	21%					79%					
PEO-Ce-LDH	B. E.	879.5	884.3	897.3	902.0		881.8	888.3	898.0	900.3	906.7	915.8
	Area ratio	0.14	0.62	1	0.28		0.86	0.58	0.09	0.40	0.31	0.74
	Content	41%					59%					
PEO-Ce-LDH-P	B. E.	879.6	884.3	897.8	902.0		881.9	888.2	897.0	900.4	906.7	915.9
	Area ratio	0.36	1	0.73	0.52		0.97	0.71	0.66	0.43	0.42	0.97
	Content	39%					61%					

Table 2 Electrochemical parameters: corrosion potential (E_{corr}), corrosion current

density (i_{corr}), anodic (b_a) and cathodic (b_c) slopes obtained from the Tafel

extrapolation method and the polarisation resistance (R_p).

	E_{corr} (V_{SCE})	i_{corr} ($\mu A.cm^{-1}$)	Tafel slope ($V.dec^{-1}$)		R_p ($\Omega \cdot cm^{-2}$)
Substrate	-1.00 ± 0.21	13.60 ± 1.2	b_a: 0.42	b_c: 0.18	4.02×10^3
PEO	-0.46 ± 0.06	2.31 ± 0.65	b_a: 6.78	b_c: 3.78	4.57×10^5
PEO-Ce	-0.37 ± 0.03	0.68 ± 0.19	b_a: 3.58	b_c: 12.94	1.79×10^5
PEO-Ce-LDH	-0.34 ± 0.04	0.51 ± 0.23	b_a: 6.28	b_c: 8.11	3.02×10^6
PEO-Ce-LDH-P	-0.13 ± 0.06	0.05 ± 0.18	b_a: 8.42	b_c: 11.46	4.22×10^7

Table 3 Fitted parameters for EIS spectrum depicted in Fig. 10.

Specimens		C_{por} (S s^n cm^{-2})	n_{por}	R_{por} (Ω cm^2)	C_{inn} (S s^n cm^{-2})	n_{inn}	R_{inn} (Ω cm^2)	C_{dl} (S s^n cm^{-2})	n_{dl}	R_{ct} (Ω cm^2)	χ^2
30 min	*PEO*	3.2×10^{-6}	0.7	2.9×10^3	7.3×10^{-2}	0.9	4.1×10^3	-	-	-	1.7×10^{-3}
	PEO-Ce	5.1×10^{-6}	0.8	3.5×10^2	1.0×10^{-7}	0.9	2.4×10^4	-	-	-	2.4×10^{-3}
	PEO-Ce-LDH	1.4×10^{-6}	0.6	7.9×10^3	5.5×10^{-6}	0.7	5.4×10^4	-	-	-	2.7×10^{-3}
	PEO-Ce-LDH-P	1.2×10^{-6}	0.5	9.3×10^3	8.9×10^{-6}	0.8	1.2×10^5	-	-	-	2.1×10^{-3}
7	*PEO*	2.1×10^{-7}	0.8	9.8×10^3	4.6×10^{-7}	0.7	1.8×10^5	2.7×10^{-5}	1	1.4×10^4	6.7×10^{-3}

days	*PEO-Ce*	1.1×10^{-6}	0.7	1.7×10^{5}	1.0×10^{-6}	0.1	5.5×10^{4}	2.1×10^{-6}	0.6	3.1×10^{5}	1.8×10^{-3}
	PEO-Ce-LDH	2.8×10^{-6}	0.1	4.3×10^{5}	3.5×10^{-7}	0.6	1.6×10^{6}	8.0×10^{-9}	1	8.9×10^{6}	4.4×10^{-3}
	PEO-Ce-LDH-P	6.1×10^{-7}	0.5	1.3×10^{4}	6.2×10^{-6}	0.4	2.1×10^{5}	4.7×10^{-6}	0.4	2.2×10^{5}	1.3×10^{-3}
21 days	*PEO*	6.0×10^{-5}	0.2	6.4×10^{2}	1.8×10^{-7}	0.6	5.5×10^{2}	9.5×10^{-5}	0.1	1.5×10^{3}	3.2×10^{-3}
	PEO-Ce	1.2×10^{-6}	0.4	1.3×10^{4}	2.7×10^{-6}	0.6	4.4×10^{5}	5.5×10^{-9}	1	3.1×10^{4}	8.4×10^{-4}
	PEO-Ce-LDH	1.7×10^{-7}	0.5	1.9×10^{4}	1.1×10^{-6}	0.6	7.1×10^{5}	8.0×10^{-6}	0.6	3.3×10^{5}	1.4×10^{-3}
	PEO-Ce-LDH-P	7.2×10^{-7}	0.3	3.0×10^{5}	7.0×10^{-7}	0.1	1.6×10^{6}	1.1×10^{-6}	0.9	4.3×10^{9}	7.7×10^{-3}